JMEPEG (2012) 21:1949–1955
DOI: 10.1007/s11665-011-0093-z

1059-9495/$19.00

Corrosion-Erosion Effect on TiN/TiAlN Multilayers

J.C. Caicedo, G. Cabrera, W. Aperador, C. Escobar, and C. Amaya

(Submitted July 27, 2010; in revised form August 10, 2011)

The goal of this work is to study electrochemical behavior under corrosion-erosion conditions for [TiN/TiAlN]$_n$ multilayer coatings with bilayer number (n) of 2, 6, 12, and 24 and/or bilayer period (Λ) of 1500, 500, 250, 150, and 125 nm deposited by a magnetron sputtering technique on Si (100) and AISI 1045 steel substrates. The Ti-N and Ti-Al-N structures for multilayer coatings were evaluated via x-ray diffraction analysis. Silica particles were used as the abrasive material in corrosion-erosion tests within the 0.5 M H_2SO_4 solution at impact angles of 30° and 90° over the surface. The electrochemical characterization was carried out using the polarization resistance technique (Tafel) to observe changes in corrosion rates as a function of the bilayer number (n) or bilayer period (Λ) and impact angle. Corrosion rate values of 359 mpy of uncoated steel substrate and 103 mpy for substrate coated with $n = 24$ ($\Lambda = 125$ nm) under an impact angle of 30° were found. On the other hand, with an impact angle of 90° the corrosion rate exhibited 646 mpy on uncoated steel substrate and 210 mpy for substrate coated with $n = 24$ ($\Lambda = 125$ nm). This behavior was related to the curves of mass loss for both coated samples and the surface damage was analyzed via SEM images for the two different impact angles. These results indicate that TiN/TiAlN multilayer coatings deposited on AISI 1045 steel are a practical solution for applications in erosive-corrosive environments.

Keywords corrosion-erosion, hard coatings, multilayers, Tafel

1. Introduction

The erosion-corrosion process is associated with current induced by mechanical surface removal of the protective film. Also, the damage rate of the substrate surface is increased in chemical or electrochemical processes. In this sense, the impact velocity and impact angle are recognized as two parameters that noticeably influence the wear rates and surface degradation in tribosystems that suffer erosion and corrosion-erosion (Ref 1-5). Surface engineering of metallic substrates with protective coatings unanimously calls to attention the industry and researchers, as it produces a host of properties such as wear protection, erosion resistance, oxidation protection, and corrosion resistance (Ref 6-10). Previous studies have reported that the concept of multilayer coatings offers a potent solution for physical, tribological, and chemical properties in hard coatings, e.g., TiN/ZrN (Ref 11), TiCN/TiNbCN (Ref 12), CrN/NbN (Ref 13), CrN/AlN (Ref 14). Moreover, when TiN/TiAlN multilayer coatings are deposited on cutting tools, this material produces high wear resistance 0.22-0.28 (Ref 15, 16). However, the literature shows a few studies about multilayer coatings tested against erosive-corrosive processes, e.g., CrN/NbN (Ref 17, 18).

In accordance with the latter, the goal of this work is to study the behavior of [TiN/TiAlN]$_n$ multilayer coatings in a corrosive-erosive fluid as a function of bilayer number (n) and bilayer period ($\Lambda = t_{TiN} + t_{TiAlN}$). To achieve the proposed objective, with an impact velocity fixed at 11.12 m/s, the impact angle in relation to wear particles was varied (30° and 90°).

J.C. Caicedo, Thin Films Group Universidad del Valle, Cali, Colombia and Advanced Materials for Micro and NanoTechnology Research Group, Universidad Autonoma de Occidente, Cali, Colombia **G. Cabrera** and **C. Escobar**, Thin Films Group Universidad del Valle, Cali, Colombia; **W. Aperador**, Ingeniería Mecatrónica, Universidad Militar Nueva Granada, Bogotá, Colombia; and **C. Amaya**, Thin Films Group Universidad del Valle, Cali, Colombia and Hard Coating Laboratory CDT-ASTIN SENA, Cali, Colombia. Contact e-mail: jcaicedoangulo@gmai.com.

2. Experimental Details

[TiN/TiAlN]$_n$ multilayer coatings have been grown onto Si (100) and AISI 1045 steel substrates using a multi-target magnetron sputtering system, with an r.f. source (13.56 MHz) and two Al and Ti metallic targets with a purity of 99.9%. The optimum deposition parameters were the following: sputtering power of 350 W for Al and 400 W for the Ti target (these deposition parameters can generate a slight non-homogeneous thickness of single layers due to the difference in the sputtering yield for Al and Ti materials); substrate temperature of 300 °C; circular rotation substrate fixed at 60 rpm; and a sputtering gas mixture of Ar 93% and N_2 7% under a total working pressure of 6×10^{-3} mbar was employed. In this work, the same nitrogen flow (3.7 sccm) was fixed for TiN and TiAlN individual layer depositions with a goal of analyzing the substitution effects when the Al ions replaced the Ti atoms. An unbalanced r.f. bias voltage, which generates a constant voltage offset of −70 V was applied. Moreover, the magnetron sputtering device had a positioning substrate system in relationship to the target spot, this parameter permitted a variation in the bilayer number (n) among 2, 6, 12, and 24; changing the bilayer period (Λ) from 1500 to 150 nm. The crystal structure of the coatings was determined using a *D8*

Advance Bruker X'ray diffractometer with Cu-Kα (λ = 1.5405 Å) radiation. Chemical composition of the coatings was determined by energy dispersive x-ray (EDX) spectroscopy using a *Philips XL 30 FEG*, therefore, a high-purity Ge EDX detector for the reliable acquisition of EDX spectra was used in this analysis. The structural assembly of the multilayers was analyzed by scanning electron microscopy (SEM) (*Philips XL 30 FEG*) equipped with a light optical magnification range: 525-24.00× and height sensitivity backscatter electron detector (EDAX-EDX) system.

For the analysis of the erosive-corrosive effect, a device built for the evaluation of chemical attacks on metallic materials and coated materials was used. Figure 1 shows the erosive-corrosive test device that consists of a tribometer with a glass container for erosive-corrosive storage, an acrylic cover that is available in the sample holder and electrodes with an impelling of *High Ultra Molecular Weight Polyethylene* (HUMWPE) which rests on a Teflon shaft that is attached to the main motor shaft which provides fluid motion. The lid of the container allows the sample to be located with exposure under angles of 30° and 90° for corrosive fluid action, as well as the reference electrode and counter-electrode. The last angle leads to locating the sample perpendicular with respect to the fluid flow. On the other hand, the fluid movement is caused by a drive shaft motor. The tangential speed applied to the fluid with erosive particles was fixed at 11.12 m/s, this took into account that the impeller radius was 0.055 m and the motor speed was fixed at 1930 rpm. The electrochemical study was carried out with a *Gamry* unit, model PCI 4 with D.C. and A.C. signals which generated the Tafel polarization curves. These curves were developed at room temperature using a cell that supports one working electrode within an exposed area (1 cm^2), this working electrode is based on carbon steel and, therefore, the equivalent weight for carbon steel is 27.92 g (*ASTM G 102-Standard Practice for calculation of corrosion rates and related information from electrochemical measurements*). A reference electrode ($Cu/CuSO_4$) and graphite counter electrode were utilized in 3.5% NaCl + 0.5 M H_2SO_4 solution with distilled water. The resting potential was measured during 30 min. The Tafel curves were taken at around 1 h. This time was necessary for an anodic and cathodic sweep potential. Tafel polarization curves were obtained at a sweep speed of 0.5 mV/s in voltage ranges from −0.2 to 0.8 V with an exposed area of 1 cm^2.

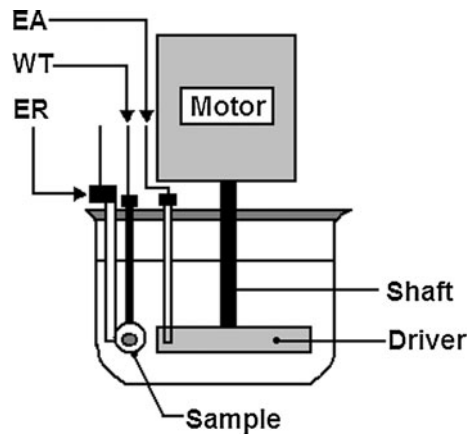

Fig. 1 Schematic for the device used at corrosion-erosion wear testing. EA, auxiliary electrodes; WE, working electrodes; RE, reference electrodes (Ref 19)

In this work, silica (SiO_2) was used as the abrasive agent, with a particle size of between 210 and 300 μm. This solution was chosen because it is used to study steel materials because it facilitates the observations at defined anodic regions and the addition of chloride which guaranteed an effective attack. Finally for the analyzed corrosion surface process, the superficial morphology was characterized using a high-resolution SEM (*Philips XL 30 FEG*).

3. Results and Discussion

3.1 X-ray Diffraction (XRD) Analysis

The total measured thickness of the deposited $[TiN/TiAlN]_n$ was found to be approximately 3 μm for all multilayers. The individual thickness varied in function with the bilayer numbers from $n = 2$ to $n = 24$ and the producing bilayer periods (Λ) from 1500 to 125 nm. Figure 2 shows the XRD pattern of TiN/TiAlN coatings deposited with $n = 1$, $\Lambda = 3$ μm; $n = 12$, $\Lambda = 150$ nm, and $n = 24$, $\Lambda = 150$ nm onto Si (100) substrate, at a r.f. negative bias voltage of −70 V.

From the XRD pattern it was possible to observe the strongest peak in a Bragg plane (220), which was associated to the Ti_3AlN cubic phase. The latter indicated a light textured growth along this orientation. Other weak peaks identified correspond to diffractions of TiN (200), Ti_3AlN (311), and (222) planes of the FCC structure. Moreover, the AlN (422), h-AlN (112) peaks for the AlN within Ti-Al-N materials are exhibited. These characteristic orientations are in agreement with the JCPDF00-038-1420 and JCPDF00-037-1140 from TiN and AlTiN ICCD cards, respectively. The presence of the Ti_3AlN (220) obtained on Ti-N layers is associated with a substitution mechanism, where Al atoms replace Ti atoms, resulting in a Ti-ordered Al-N disordered FCC NaCl-type structure in which Ti and Al atoms are placed at the Wyckoff site 4a, while N atoms randomly occupied the Wyckoff site 4b (Ref 20). This means that the nitrogen gas flow rate directly

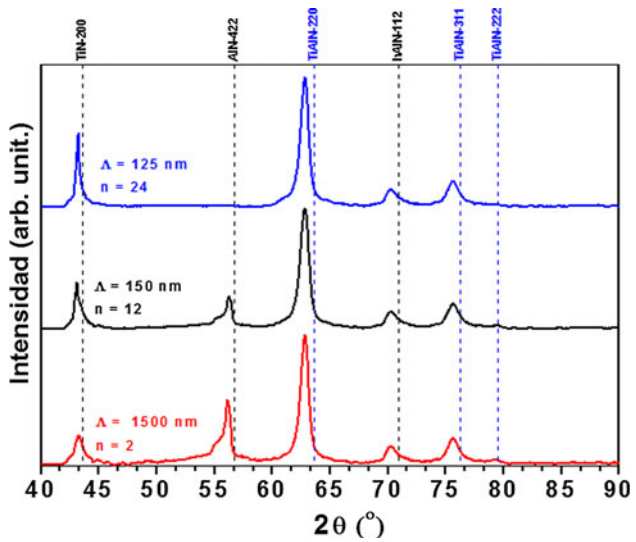

Fig. 2 XRD patterns for TiN/TiAlN multilayers grown with $n = 2$, $n = 12$, and $n = 24$. Dashed lines indicate the positions of the peaks obtained from JCPDF00-038-1420 and JCPDF00-037-1140 files from ICCD cards

influences the structure of Ti-Al-N coatings. When the nitrogen gas flow rate is around 3.7 sccm it facilitates Al access to the deposition surface; hence, the FCC structure is determined by a partially ordered structure with Ti atoms, creating vacancies in non-metallic sub lattices (Ref 20).

Regarding the lattice parameter, obtained from the preferential orientation in the TiN and AlTiN single-layered coatings as well as was the multilayered system with bilayer periods Λ = 250 nm (n = 12), in this study the *Nelson-Riley* extrapolation technique was employed in the refinement procedure to determine the value of a_0 ($\pm$0.0001 nm), because this technique permits direct precision determination of the lattice constant (Table 1). From the table results it is possible to observe an expansion of the cell unit related to the value reported in the literature for $Ti_{1-x}Al_xN_y$ powder ($Ti_{0.1}Al_{0.1}N_{0.8}$) compared to the Ti-Al-N coating deposited with a r.f. negative bias voltages of $-$70 V. This creates a mismatch effect with the Ti-N layer, since the latter has a lattice parameter of 0.4240 nm. It was also observed that the multilayer system showed less of a residual stress than those of single layers; this release stress effect is due to the interfaces which are characteristic of those multilayered systems (Ref 12).

On the other hand, a careful correction has to be done in all stoichiometric analyses because EDX has low reliability in nitrogen concentration. Therefore, EDX elemental concentrations were obtained using the ZAF correction method; because certain factors related to the sample composition called matrix effects associated with atomic number (Z), absorption (A), and fluorescence (F)) can affect the x-ray spectrum produced during the analysis of electron microprobes, therefore, these effects should be corrected to ensure the development of an appropriate analysis. The correction factors for a standard specimen of known compositions were determined initially by the ZAF routine. The relative intensity of the peak K was determined by dead time corrections and a referent correction for the x-ray measured. So, before each quantitative analysis of an EDX spectrum, a manual background correction and an automated ZAF correction was carried out (Ref 11). Thus, Table 1 shows the EDX spectroscopy values of TiN_x and $Ti_{1-x}Al_xN_y$ single layers, respectively, deposited with an r.f. negative bias voltage of $-$70 V. All samples were observed via SEM and chemical analyses were done with an amplification of 20,000$\times$.

3.2 SEM Analysis

A first glimpse at TiN/TiAlN multilayer modulations and microstructure was accomplished by SEM micrographs. Figure 3 presents the cross-sectional image of a TiN/TiAlN coating with n = 24 (Λ = 125 nm). The darkest contrast of TiAlN layers with respect to the TiN ones allowed a clear determination of the layers structure. These TiN/TiAlN coatings presented a well-defined and uniform periodicity. All the multilayer stacks were resolved by SEM and confirmed quite precisely the previously designed values of bilayer thickness, as well as the total thicknesses. The only slight deviation observed by SEM imaging was in the relative nanometric thicknesses. In this specific sample, TiAlN layers seem to be a little bit thicker than TiN ones. These deviations are difficult to evaluate because of the poor resolution of the TiN/TiAlN interfaces in this technique.

3.3 Corrosion-Erosion Analysis

For the corrosion rate analysis, the corrosion velocity was calculated after the previous determination of the current corrosion density, j_{corr}, using the *Stern-Geary* equation:

$$j_{corr} = \frac{\beta_a \cdot \beta_c}{2.303 R_t^T (\beta_a + \beta_c)} \quad \text{(Eq 1)}$$

where R_t^T is the polarization resistance and β_a and β_c are the anodic and cathodic Tafel slopes, respectively. To determine β_a and β_c, a potentiodynamic sweeping was conducted using the Tafel technique. Finally, the corrosion velocity, V_{corr}, can be expressed as:

$$V_{corr} = \frac{j_{corr} \cdot K \cdot E_w}{A \cdot d} \quad \text{(Eq 2)}$$

where K is proportionality constant, E_w is the weight of the work electrode (the equivalent weight for carbon steel is

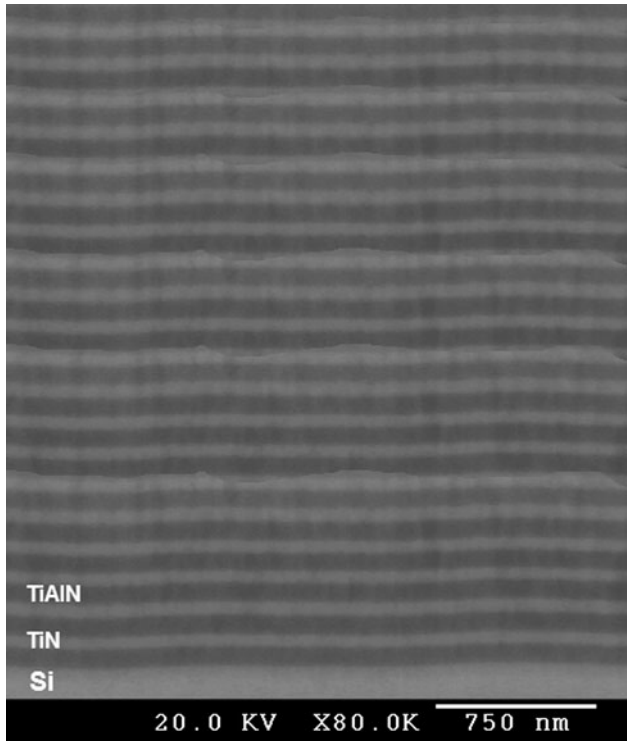

Fig. 3 SEM micrograph of $[TiN/TiAlN]_n$ with Λ = 125 nm

Table 1 Stoichiometric relationship analyzed by EDX with subtractions of oxygen contribution and lattice parameter of TiN and Ti3AlN single layer coatings

Negative r.f. bias voltage, V	Binary coatings ($Ti_{1-x}N_x$)	a_0, nm, FCC (111) ($Ti_{1-x}N_x$)	Ternary coatings ($Ti_{1-x}Al_xN_y$)	a_0, nm, FCC (220) ($Ti_{1-x}Al_xN_y$)
$-$70	$Ti_{0.4}N_{0.6}$	0.4240	$Ti_{0.14}Al_{0.15}N_{0.71}$	0.4175

27.92 g) (Ref 21). The general results of corrosion rate in multilayer coatings with impact angles of 30° and 90° are shown in Table 2.

Tafel polarization curves are shown in Fig. 4 and 5. These curves allowed for determination of the values of the anodic and cathodic Tafel slopes, which are necessary to calculate an accurate value of the corrosion rate. For impact angles of 30° and 90°, a similar shape is observed in the five polarization curves, with a plateau on the cathodic branch controlling the corrosion process which may be associated with an oxygen reduction mechanism. After the plateau the rest potential (E_{corr}) is defined together with the pitting potential (E_{pit}). Thus, the anodic branch does not show a passive plateau where the coatings generate a displacement of the curves towards lower values of the current density and potentials more noble than that steel substrate. This behavior is related to the increase of the bilayer number (n) and a decrease in the bilayer period (Λ), showing that the larger bilayer number and lower bilayer period in the multilayer coatings responds better against the corrosive-erosive effects (Ref 22, 23).

Figure 4 shows the values of the corrosion rate in function with the bilayer number (n) and bilayer period (Λ), in corrosion-erosion conditions to impact angles of 30°. The curves showed a tendency towards lower values with an increase in the bilayer number and decrease in the bilayer period. These types of coatings generate a great number of interfaces such as was shown by SEM results, which are regions that present structural disorder and marked changes in crystallographic orientation as was discussed in the XRD analysis, therefore, those interfaces can act as obstacles for the inward and outward diffusions of Cl^- ion species, generating an increment in the energy or potential required for translating the corrosive ions across the coating/substrate interface. The corrosion rate values for the impact angle of 90° in Fig. 5 presents a higher corrosion rate than with those having an impact angle of 30°. This effect is observed in samples that exhibited twice the corrosion rate than those multilayer coatings attacked with an angle of 30°. The reason for this fact is due to those normal angles, the particle struck with great energy on surfaces causing significant wear to the material. It was discovered that the coating deposited with $n = 24$ ($\Lambda = 125$ nm) under an impact angle of 90° provides corrosion rates 2 times higher than that which was tested at a lower impact angle of 30°. The general trend was to reduce the corrosion rate when the interface numbers are increased, generated by increasing of the bilayer number (n) and reduction of bilayer period (Λ). Finally, Fig. 6 shows the corrosion rate in function with the bilayer number. It is observed that the highest impact angle (90°) exhibited a dramatic increase in corrosion rate in all cases.

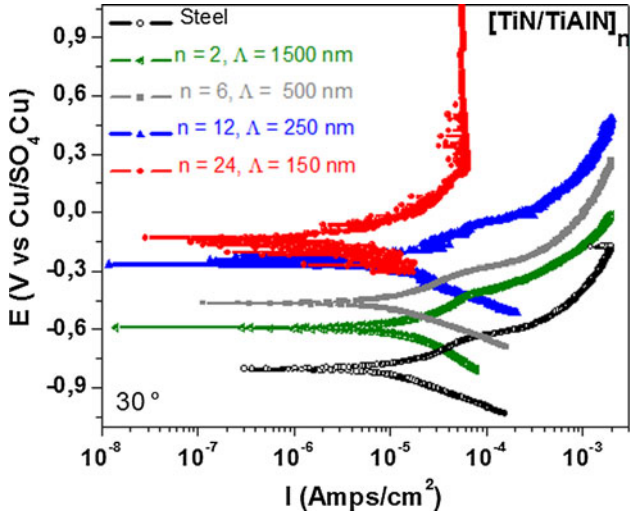

Fig. 4 Tafel curves of corrosion-erosion with an impact angle of 30°

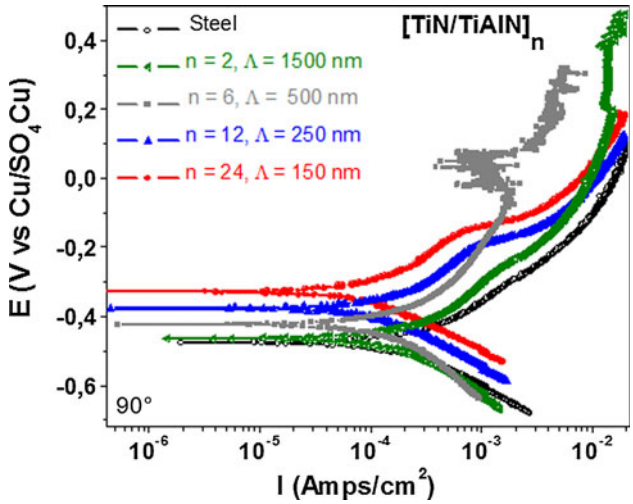

Fig. 5 Tafel curves of corrosion-erosion with an impact angle of 90°

Table 2 Parameters used to calculate the corrosion rate with different impact angles (30° and 90°)

	Steel	$n = 2$	$n = 6$	$n = 12$	$n = 24$
30°					
Corrosion potential, mV	−799.23	−589.41	−459.48	−266.17	−132.99
β_a, mV/decade	−0.378	−0.270	−0.243	−0.223	−0.169
β_c, mV/decade	−0.343	0.280	0.289	0.212	0.174
j_{corr}, μA/cm^2	791.9	604.1	545.0	329.8	228.0
V_{corr}, mpy	359.17	274.01	247.2	149.59	103.42
90°					
Corrosion potential, mV	−0.474	−0.463	−0.421	−0.375	−0.328
β_a, mV/decade	−0.422	−0.347	−0.314	−0.295	−0.241
β_c, mV/decade	0.412	0.321	0.312	0.265	0.217
j_{corr}, μA/cm^2	1420.0	738.6	573.4	505.3	465.0
V_{corr}, mpy	646.28	335.00	260.09	229.17	210.91

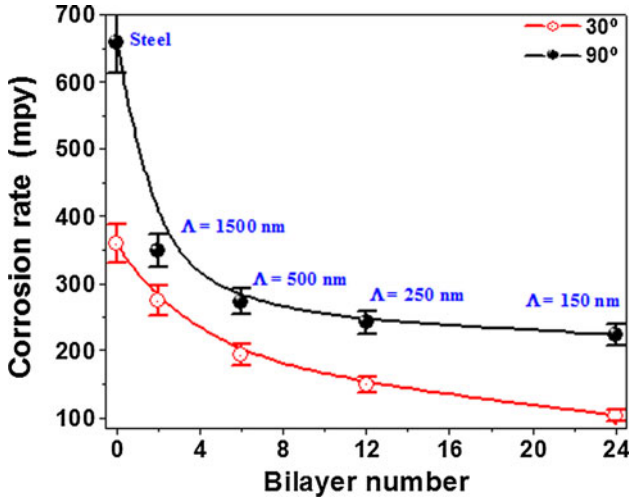

Fig. 6 Corrosion rate in function with bilayer numbers for two different impact angles

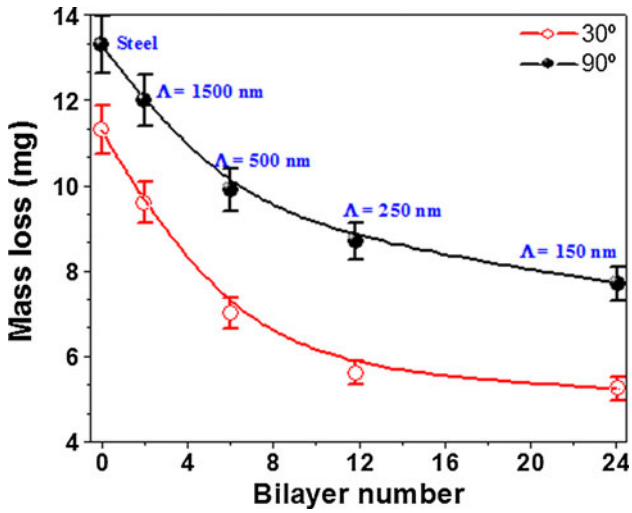

Fig. 7 Mass loss versus bilayer number for two impact angles

The wear indicator like mass loss related to corrosive-erosive system is shown Fig. 7. In this work noted was a decrease in wear rate is in relation to a decrease in the corrosion rate provided by multilayer coatings. This is due to two cooperative effects. First being, multilayer coatings exhibit a higher hardness because the load is absorbed and distributed in a better manner across the interfaces between different materials such as TiN and TiAlN layers (Ref 24). The last physical effect generates an increase in mechanical toughness of multilayer coatings. The second cooperative effect is in relation to high corrosion resistance which offers a reduction in corrosive attacks from Cl^- ions.

In uncoated samples (steel 1045), observed was delamination in punctual zones on the steel substrate surface because of poor mechanical and anticorrosive properties compared to $[TiN/TiAlN]_n$ multilayers. The mass loss decreases for both angles measured in steel coated with increasing bilayer numbers (n) and a reduction of bilayer periods (Λ) in relation to uncoated steel, indicating good performance for these multilayer coatings under corrosive-erosive conditions. Moreover, in this work was confirmed that corrosion-erosion strongly depends of the impact angle due to the change in the impact energy when the particles changes form 30° to 90°.

4. Surface Analysis After Erosive-Corrosive Attack

SEM micrographs are shown in Fig. 8 and 9 for uncoated steel substrate and $[TiN/TiAlN]_n$ nanometric multilayer deposited with $n = 24$ ($\Lambda = 125$ nm) on steel substrate under corrosion-erosion processes for two impact angles. For an impact angle of 30°, Fig. 8(a) shows the uncoated steel with a crack that had been generated by wear mechanisms. The white areas reflect the surface damage caused by the corrosion attack. Figure 8(b) shows a surface without fracture which exhibits the protection afforded by multilayer coating on steel substrate.

For impact angles of 90°, Fig. 9(a) shows the surface of uncoated steel substrate indicating a more aggressive attack than the impact angles of 30° thus creating high corrosive wear. Figure 9(b) shows a fractured surface in which the coating has

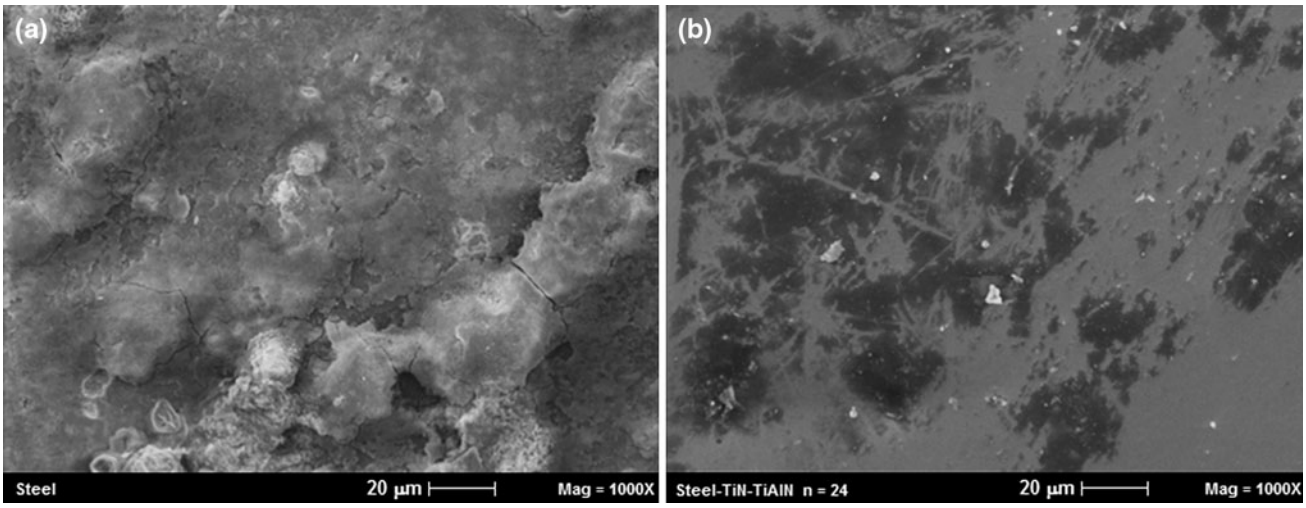

Fig. 8 SEM micrographs for samples under corrosion-erosion processes (a) uncoated steel, (b) steel/$[TiN/TiAlN]_{24}$ with an impact angle of 30°

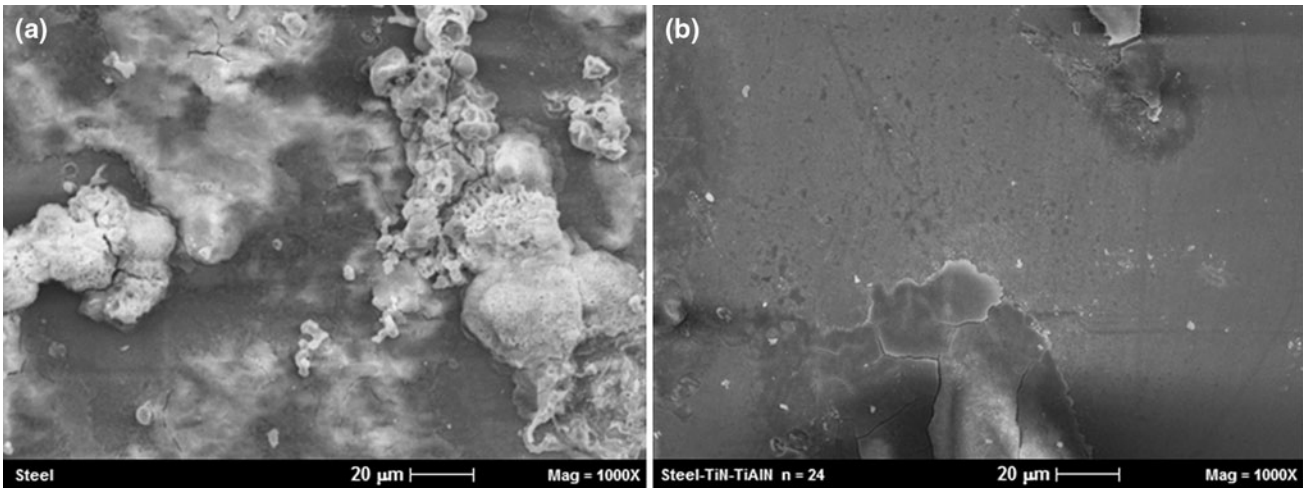

Fig. 9 SEM micrographs for samples under corrosion-erosion processes (a) steel, (b) steel/$[TiN/TiAlN]_{24}$ with an impact angle of 90°

been delaminated due to an abrasion phenomenon caused by energetic particles that impact in normal angles of (90°) on $[TiN/TiAlN]_n$ surfaces thus showing the great aggressive effect.

5. Summary

$[TiN/TiAlN]_n$ multilayer coatings were deposited by reactive r.f. magnetron sputtering using simultaneous deposition from Al and Ti targets in N_2 + Ar mixtures. The XRD pattern confirmed the formation of the TiN_x binary and Ti_3-Al-N ternary phases in nanostructured multilayer coatings.

The $[TiN/TiAlN]_n$ multilayer coatings improves the performance for AISI 1045 steel under corrosion-erosion processes, such as was presented by Tafel curves of two different impact angles. Wear corrosion mechanisms found after corrosion-erosion tests were micro-cutting and micro-plow for an impact angle of 30°; finally, the generation of craters and surface cracking for an impact angle of 90° were determined as the highest aggressive effect and observed by SEM micrographs.

The increase of bilayer number (n) and the decrease of bilayer period (Λ) in the nanometric multilayer coatings allow for the improvement of resistance to corrosion under corrosive-erosive conditions. Moreover, the normal impact angle of 90° showed the highest values of corrosion rates compared to an impact angle of 30°.

Acknowledgments

This research was supported by "El patrimonio Autónomo Fondo Nacional de Financiamiento para la Ciencia, la Tecnología y la Innovación Francisco José de Caldas" under contract RC-No. 275-2011 with the Center of Excellence for Novel Materials (CENM) at the Universidad del Valle in Cali, Colombia.

References

1. L.R. Katipelli, A. Agarwal, and N.B. Dahotre, Interfacial Strength of Laser Surface Engineered TiC Coating on 6061 Al Using Four-Point Bend Test, *Mater. Sci. Eng. A*, 2000, **289**, p 34
2. U. Helmersson, S. Todovora, S.A. Barnett, J.S. Sundgren, H. Markett, and J.E. Greene, Growth of Single-Crystal TiN/VN Strained-Layer Superlattices With Extremely High Mechanical Hardness, *J. Appl. Phys.*, 1987, **62**, p 481
3. C.J. Tabares, L. Rebouta, B. Almeida, J. Bessa e Sousa, M.F. da Silva, and J.C. Soares, Deposition and Characterization of Multilayered TiN/ZrN Coatings, *Thin Solid Films*, 1998, **317**, p 124
4. T.S. Li, H. Li, and F. Pan, Microstructure and Nanoindentation Hardness of Ti/TiN Multilayered Films, *Surf. Coat. Technol.*, 2001, **137**, p 225
5. J. Smolik and K. Zdunek, Effect of Interlayer Composition on the Tribological Properties of TiC/Ti(C_x, N_{1-x})/TiN Anti-Abrasive Multi-Layer Coatings, *Vacuum*, 1999, **55**, p 147
6. J.C. Caicedo, C. Amaya, L. Yate, W. Aperador, G. Zambrano, M.E. Gómez, J. Alvarado-Rivera, J. Muñoz-Saldaña, and P. Prieto, Effect of Applied Bias Voltage on Corrosion-Resistance for $TiC_{1-x}N_x$ and $Ti_{1-x}Nb_xC_{1-y}N_y$ Coatings, *Appl. Surf. Sci.*, 2010, **256**, p 2876
7. L. Yate, J.C. Caicedo, A. Hurtado Macias, F.J. Espinoza-Beltrán, G. Zambrano, J. Muñoz-Saldaña, and P. Prieto, Composition and Mechanical Properties of AlC, AlN and AlCN thin Films Obtained by r.f. Magnetron Sputtering, *Surf. Coat. Technol.*, 2009, **203**, p 1904
8. J.E. Sanchéz, O.M. Sanchéz, L. Ipaz, W. Aperador, J.C. Caicedo, C. Amaya, M.A. Hernández Landaverde, F. Espinoza Beltran, J. Muñoz-Saldaña, and G. Zambrano, Mechanical, Tribological, and Electrochemical Behavior of $Cr_{1-x}Al_xN$ Coatings Deposited by r.f. Reactive Magnetron Co-Sputtering Method, *Appl. Surf. Sci.*, 2010, **256**, p 2380
9. C. Amaya, W. Aperador, J.C. Caicedo, F.J. Espinoza-Beltrán, J. Muñoz-Saldaña, G. Zambrano, and P. Prieto, Corrosion study of Alumina/Yttria-Stabilized Zirconia (Al_2O_3/YSZ) Nanostructured Thermal Barrier Coatings (TBC) Exposed to High Temperature Treatment, *Corros. Sci.*, 2009, **51**, p 2994
10. M. Grizalez, E. Martínez, J.C. Caicedo, J. Heiras, and P. Prieto, Occurrence of Ferroelectricity in Epitaxial $BiMnO_3$ Thin Films, *Microelectron. J.*, 2008, **39**, p 1308
11. J.C. Caicedo, C. Amaya, L. Yate, O. Nos, M.E. Gómez, and P. Prieto, Hard coating Performance Enhancement by Using $[Ti/TiN]_n$, $[Zr/ZrN]_n$ and $[TiN/ZrN]_n$ Multilayer System, *Mater. Sci. Eng. B*, 2010, **171**, p 56
12. J.C. Caicedo, C. Amaya, L. Yate, G. Zambrano, M.E. Gómez, J. Alvarado-Rivera, J. Muñoz-Saldaña, and P. Prieto, TiCN/TiNbCN Multilayer Coatings with Enhanced Mechanical Properties, *Appl Surf. Sci.*, 2010, **256**, p 5898
13. S.-K. Tien, J.-G. Duh, and J.-W. Lee, Oxidation Behavior of Sputtered CrN/AlN Multilayer Coatings During Heat Treatment, *Surf. Coat. Technol.*, 2007, **201**, p 5138
14. J. Lin, J.J. Moore, B. Mishra, M. Pinkas, X. Zhang, and W.D. Sproul, CrN/AlN Superlattice Coatings Synthesized by Pulsed Closed Field Unbalanced Magnetron Sputtering with Different CrN Layer Thicknesses, *Thin Solid Films*, 2009, **517**, p 5798
15. A. Vladescu, A. Kiss, M. Braic, M. Balaceanu, C. Iordachel, L. Buia, and V. Braic, Nanostructured Multilayer Nitride Coatings for

Biocompatible Materials, *European Cells and Materials*., 2006, **11**(Suppl. 2), p 36
16. C.-H. Hsu, M.-L. Chen, and K.-L. Lai, Corrosion Resistance of TiN/TiAlN-Coated ADI, by Cathodic Arc Deposition, *Mater. Sci. Eng. A*, 2006, **421**, p 182–190
17. Y.P. Purandare, M.M. Stack, and P.Eh. Hovsepian, Velocity Effects on Erosion-Corrosion of CrN/NbN "Superlattice" PVD Coatings, *Surf. Coat. Technol.*, 2006, **201**, p 361–370
18. M.M. Stack, Y. Purandare, and P. Hovsepian, Impact Angle Effects on the Erosion-Corrosion of Superlattice CrN/NbN PVD Coatings, *Surf. Coat. Technol.*, 2004, **188**, p 556–565
19. M.G. Fontana, *Corrosion Engineering*, McGraw-Hill, New York, 1986
20. Z.J. Liu, P.W. Shum, and Y.G. Shen, Hardening Mechanisms of Nanocrystalline Ti–Al–N Solid Solution Films, *Thin Solid Films*, 2004, **468**, p 161
21. ASTM G 102-Standard Practice for Calculation of Corrosion Rates and Related Information from Electrochemical Measurements
22. M. Stern and A.L. Geary, Electrochemical Polarization: I. A Theoretical Analysis of the Shape of Polarization Curves, *J. Electrochem. Soc.*, 1957, **104**(1), p 56–63
23. V.K. William Harish, C. Barshilia, V. Ezhil Selvi, Kalavati, and K.S. Rajam, Electrochemical Behavior of Single Layer CrN, TiN, TiAlN Coatings and Nanolayered TiAlN/CrN Multilayer Coatings Prepared by Reactive Direct Current Magnetron Sputtering, *Thin Solid Films*, 2006, **514**, p 204–211
24. A. Afrasiabi, M. Saremi, and A. Kobayashi, A Comparative Study on Hot Corrosion Resistance of Three Types of Thermal Barrier Coatings: YSZ, YSZ + Al_2O_3 and YSZ/Al_2O, *Mater. Sci. Eng. A*, 2008, **478**, p 264–269